

Impact of Local Structure on Halogen Ion Migration in Layered Methylammonium Copper Halide

Memory Devices

Aniruddha Ray,^{†‡#} Beatriz Martín-García,^{‡∇#} Alberto Martinelli,^{‡#} Davide Spirito,[§] Federico Locardi,^{‡‡} Davide Altamura[♦], Cinzia Giannini[♦], Mirko Prato,^Δ Liberato Manna,^{†*} and Ahmed L. Abdelhady^{†*}

[†]Nanochemistry Department, [‡]Graphene Labs and ^ΔMaterials Characterization Facility, Istituto Italiano di Tecnologia, Via Morego 30, 16163 Genova, Italy

^{‡‡}Dipartimento di Chimica e Chimica Industriale, Università degli Studi di Genova, Via Dodecaneso, 31, 16146, Genova, Italy

[∇]CIC nanoGUNE, Tolosa Hiribidea 76, 20018 Donostia-San Sebastian, Basque Country, Spain.

^{‡‡}SPIN-CNR, C.so Perrone 24, I-16152 Genova, Italy

[§]IHP—Leibniz-Institut für innovative Mikroelektronik, Im Technologiepark 25, D-15236 Frankfurt (Oder), Germany

^{‡‡}Physics and Chemistry of Nanostructures (PCN), Ghent University, Krijgslaan 281 - building S3 (Campus Sterre), 9000 Gent, Belgium

[♦]Istituto di Cristallografia, Consiglio Nazionale delle Ricerche, v. Amendola 122/O, 70126 Bari, Italy

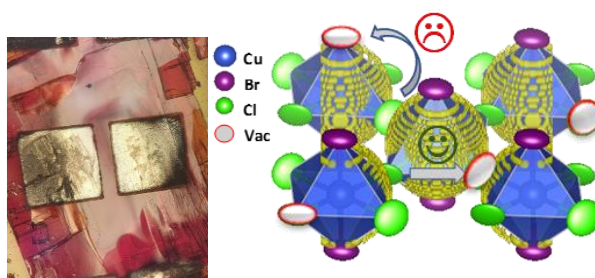
[#]Contributed equally.

^{*}Corresponding author(s): liberato.manna@iit.it and ahmed.abdelhady@iit.it

Abstract

Ion migration is associated with hysteresis observed in halide perovskite-based solar cells and light-emitting diodes, however, it is crucial for their effective performance in memory devices. In the halide perovskites field, a direct link between the average/local structure and the preferred ion migration hopping pathway has yet to be established. Herein, we utilize the solvent acidolysis crystallization technique to grow various halide-deficient methylammonium copper halide crystals where perovskite-type layers are found. Through synchrotron X-ray powder diffraction (XRPD) and pair distribution function (PDF) analyses, we identify the halogen vacancy site in the copper halide octahedra, the octahedra tilting, and the thermal vibrations of the atoms around their average positions. We correlate the variations in these parameters to the hysteresis observed in the current-voltage curves and subsequently to the ON/OFF ratios of proof-of-concept memory devices fabricated using inert Pt electrodes. Furthermore, our best ON/OFF ratio of ~ 10 from our Pb-free devices compares well to the results obtained from two-dimensional Pb-based devices utilizing inert electrodes.

TOC



Introduction

Three-dimensional (3D) hybrid lead halide perovskites (APbX_3 ; A = methylammonium (MA) or formamidinium (FA) and X = Cl, Br, or I) show significant room-temperature ion migration under external electric field, which is being increasingly accepted as one of the major origins of the current-voltage hysteresis in solar cells and light-emitting diodes.¹⁻⁶ The resulting mixed ionic-electronic conductivity in halide perovskites is now being taken advantage of in resistive switching devices, where a change in the material's resistance is induced by applying an external voltage stimulus.^{7,8} Thus, the device passes from a high resistance state (HRS, known as OFF state) to a low resistance state (LRS, known as ON state). This change allows to “write” (set process) and “erase” (reset process), resulting in a resistive random access memory (ReRAM) device. In general, the proposed working mechanism for perovskite-based ReRAM devices varies from halogen ion/vacancy migration inside the active perovskite material to the formation of metallic filaments when using active electrodes. In addition, the interactions at the perovskite-electrode interface also play an important role and must be taken into consideration.^{9,10} In all cases, ionic mobility, as well as the choice of the active electrode, have been identified as the factors enhancing the device performance in terms of ON/OFF ratio. Ionic mobility can be influenced by structural variations. For instance, local lattice distortion by bromine¹¹ or guanidinium¹² incorporation into MAPbI_3 was proposed to raise the activation energy for iodine ion migration. These activation energy values can be estimated through experimental measurements^{5,13,14} or by computation.^{13,15,16} However, the reported activation energy values, for the same ion, differ significantly.^{17,18} Importantly, the correlation between the average/local structure and the preferred ion/vacancy hopping pathway has been achieved primarily through computational calculations^{13,19-21}, while a direct structural characterization of the vacancies location and concentration as well as the atomic displacement is still missing. Nevertheless, Minns *et al.*²² have demonstrated the ion migration mechanism in MAPbI_3 through neutron diffraction measurements.

One of the main drawbacks of the commonly used 3D perovskites, both in optoelectronics and ReRAM applications, is the lead toxicity. More environmentally friendly 3D perovskites have been developed using tin²³; however, tin instability is notorious due to its facile oxidation, which yet remains an unsolved issue. Recently, the two-dimensional (2D) analog (A_2PbX_4)²⁴, which could possess different energy barrier migration pathways

compared to 3D perovskites¹⁹, are being proposed as promising candidates for memory devices.⁷ Interestingly, the size constraint placed on the metal ion is relaxed by moving to this 2D analogue, allowing the exploration of lead-free alternatives besides the commonly studied tin. In particular, copper is considered as a cheap and nontoxic element, which, if incorporated in devices, could have a significant impact even with low efficiencies; for example, layered hybrid copper halides are now finding applications in solar cells²⁵ and batteries.²⁶ Furthermore, these compounds have been recently utilized in resistive switching devices.²⁷

The crystal structure of the 2D MA₂CuCl₄ (MA = CH₃NH₃⁺) has been the subject of previous investigations with inconsistent results. Steijger *et al.*²⁸ reported a sequence of structural transitions in the 1.5 K – 400 K thermal range, summarized as follows: at T < 170 K the structure is monoclinic, between 170 K – 260 K a monoclinic and an orthorhombic polymorph coexist, while between 260 K – 348 K the orthorhombic phase is stable, and at T = 348 K an orthorhombic to tetragonal structural transition occurs. It was also argued that the orthorhombic-to-monoclinic transition is accompanied by a thermochromic transition from a light yellow to a pale green.^{29,30} Conversely, Pabst *et al.*³¹ found a monoclinic structure in the thermal range 100 K < T < 297 K and ascribed the orthorhombic pseudo-symmetry observed at room temperature by Steijger *et al.* to the presence of a domain structure. Moving to mixed halides, the MA₂CuCl₂Br₂ composition is reported to crystallize with an orthorhombic structure at room temperature with Br ions occupying the axial sites in the [CuX₆]⁴⁻ octahedra.³² Fundamental understanding of the crystal structure and its modification by the Br incorporation in these MA₂CuCl_xBr_{4-x} materials is important. Nevertheless, an accurate interpretation of the local structure could be even more crucial, mainly since ReRAM devices function via ion/vacancy migrations that are strongly influenced by local atomic structural variations, as has been demonstrated in oxide perovskites.^{33,34}

Herein, we utilized the solvent acidolysis crystallization (SAC) technique^{35,36} to grow three halide-deficient methylammonium copper halide crystals; pure chloride and two mixed chloride/bromide compositions. As the bromine content increased, the bandgaps of the crystals narrowed along with a decrease in their thermal stability. X-ray powder diffraction (XRPD) and pair distribution function (PDF) analyses using synchrotron radiation were applied to determine the average and local crystal structure of all samples at room temperature. The pure chloride sample adopted the monoclinic structure with corrugated [CuCl₆]⁴⁻ octahedra in which chlorine vacancies are

slightly higher in the equatorial in-plane octahedral positions compared to the axial sites. Both mixed halide compositions, instead, crystallized in the orthorhombic structure with flatter octahedral planes. Importantly, at the lower Br incorporation level, Br ions selectively occupy the axial positions of the octahedra, whereas Cl ions are confined to the equatorial in-plane positions that possess similar vacancy concentration compared to the equatorial sites in the pure Cl crystal. On the other hand, as the Br content increased further, the equatorial positions became almost fully occupied by Cl and Br ions, with vacancies mainly concentrated in the axial positions that are typically Br-sites. All three samples are characterized by quite large values of thermal parameters associated to halogen ions. In particular, dynamic disorder is evident mainly for the equatorial Cl ions in the sample with the lower Br incorporation level, while it is more evident for the axial halide ions in the two other samples. Finally, we fabricated proof-of-concept memory devices from mechanically exfoliated crystal flat chips using inert Pt electrodes. We found that the incorporation of a small amount of Br led to higher hysteresis in the current-voltage (I-V) curves and better device performance in terms of ON/OFF ratio, which is correlated to the aforementioned average and local structural variations.

Experimental

Materials. $\text{CuCl}_2 \cdot 2\text{H}_2\text{O}$ (99+%, Alfa-Aesar), *N*-methylformamide (NMF, 99%, Sigma-Aldrich), HBr (48% aqueous, Sigma-Aldrich) and HCl (37% aqueous, Sigma-Aldrich).

Synthesis of MA_2CuCl_4 and mixed halide $\text{MA}_2\text{CuCl}_x\text{Br}_{4-x}$ crystals. Pure chloride (Cu-1) crystals were synthesized by dissolving 1M $\text{CuCl}_2 \cdot 2\text{H}_2\text{O}$ in a mixed solvent system consisting of hydrochloric acid and NMF (1:1 by vol) then 1 mL of the solution was placed in a 20 mL vial and left undisturbed for 24 h. Crystals with lower bromine content (Cu-2) were obtained by dissolving the same concentration of 1M $\text{CuCl}_2 \cdot 2\text{H}_2\text{O}$ in mixed solvents of hydrobromic acid, hydrochloric acid, and NMF (1:1:2 by vol), and crystals were collected after three days. Finally, crystals with higher incorporation of bromine (Cu-3) were grown in seven days by dissolving again 1M $\text{CuCl}_2 \cdot 2\text{H}_2\text{O}$, this time in a mixture of hydrobromic acid and NMF (3:1 by vol). All crystals were collected on filter paper and dried for 24 h in a vacuum oven kept at 40 °C.

Characterization. Laboratory X-ray powder diffraction (XRPD) was performed using a PANalytical Empyrean X-ray diffractometer equipped with a 1.8 kW Cu K α ceramic X-ray tube and a PIXcel^{3D} 2 \times 2 area detector, operating at 45 kV and 40 mA. Powders of the ground crystals were studied under ambient conditions using a parallel beam geometry. XRPD data were analysed using the HighScore 4.1 software from PANalytical. Step sizes of 0.013 $^\circ$ and scan speeds of 0.013 $^\circ$ /s were used for the scans, respectively. Absorbance measurements for the powder samples were carried out in a Cary 5000 spectrometer using the diffuse reflectance accessory. Ultraviolet photoelectron spectroscopy (UPS) analyses were performed on ground powders to estimate the position of the valence band maximum (VBM) of the material under investigation with respect to the vacuum level. The measurements were carried out with a Kratos Axis Ultra^{DLD} spectrometer, using a He I (21.22eV) discharge lamp, on an area of 55 μ m in diameter, at a pass energy of 5eV and with a dwell time of 100 ms.

Wide Angle X-ray Scattering (WAXS) experiments were performed by a Rigaku three pinholes camera, coupled to an Fr-E+ superbright rotating anode microsource (Cu K α , λ = 0.15405 nm) through a focusing Confocal Max Flux optics (CMF 15-105).³⁷ Beam footprint was 0.2 mm (diameter). Sample-to-detector distance was 28 mm, calibrated by LaB₆ powder standard. The sample was raster scanned with a 0.2 mm lateral step, in order to obtain an average pattern from a large crystal volume. 2D WAXS data were centered and calibrated using LaB₆ standard and the corresponding 1D WAXS profiles were derived by SUNBIM software.³⁸

Differential Thermal Analysis/Thermogravimetry coupled with Gas – chromatography and Mass Spectrometry (DTA/TG and GC – MS). DTA/TG analysis (LabsysEvo 1600 – Setaram) was performed from 40 to 800 $^\circ$ C, with a heating rate of 10 $^\circ$ C/min in He (20 mL/min). The sample (~ 10 mg) was put into an open alumina crucible. Every minute the autoinjector, set at 280 $^\circ$ C (Automation – Advanced Lab Solutions), collected for 10 seconds, in a loop of 1 mL, the evolved gas from the outlet of DTA/TG. The so collected molecules were injected into the GC (TraceGC Ultra – ThermoFisher): oven and inlet temperature, 180 $^\circ$ C and 280 $^\circ$ C respectively, carrier gas He 1.2 mL/min, split ratio 1:10 and split flow 12 mL/min, column Mega-5 (5%Phenyl – 95% Methyl polisiloxane). The GC was coupled to a MS – quadrupole (DSQ I – ThermoFisher) operating in the EI mode (70 eV), ion source at 250 $^\circ$ C, transfer line at 280 $^\circ$ C. The MS scanning was performed in the m/z range 10 – 200. The experimental conditions allowed a distinguishable separation between the different features and their attribution.³⁹ The mass

spectra identification was performed using the NIST Mass Spectral Search Program for the NIST/EPA/NIH Mass Spectral Library Version 2.2.

Synchrotron X-ray powder diffraction (XRPD) and Pair Distribution Function (PDF) analyses. Synchrotron X-ray elastic scattering experiments were carried out at the ID22 beamline of the European Synchrotron Radiation Facility (ESRF; Grenoble, France); data were collected at 297 K. Samples were analyzed by X-ray powder diffraction (XRPD) using a wavelength $\lambda = 0.400 \text{ \AA}$. Structural refinements were carried out according to the Rietveld method⁴⁰ using the FullProf (FP) program; in particular, a file describing the instrumental resolution function, and a Thompson-Cox-Hastings pseudo-Voigt convoluted with axial divergence asymmetry function were used during calculations. In the final cycle, the following parameters were refined: the scale factor; the zero point of detector; the background; the unit cell parameters; the atomic site coordinates not constrained by symmetry (H atoms were excluded from the structural model); the atomic displacement parameters; the anisotropic strain parameters; and the atomic occupations of Cu, Cl and Br atoms. Pair distribution function (PDF) data were collected using a wavelength $\lambda = 0.2065 \text{ \AA}$. Data from an empty borosilicate capillary were collected to subtract the container scattering; moreover, a standard LaB₆ sample was analyzed using the same experimental conditions in order to describe the experimental resolution effects. Reduction of the total scattering data to obtain $G(r)$, the reduced PDF, and $S(Q)$, the total-scattering structure function, was achieved by the PDFgetX3 software⁴¹ using $Q_{\max} = 25.0 \text{ \AA}^{-1}$, a range sufficient for an accurate analysis.⁴² Full-profile fitting of the $G(r)$ function was carried out using the PDFgui software⁴³ and the structural parameters obtained by the Rietveld refinements as starting structural models. In the last cycle of the fitting the following parameters were refined: the scale factor; the unit cell parameters; the atomic positions not constrained by symmetry; the anisotropic atomic displacement parameters according to the space group symmetry (for C and N atoms only the isotropic atomic displacement parameters were considered); the dynamic correlation factor. The parameters describing the experimental resolution effects (Q_{damp} and Q_{broad}) were fixed to the values refined using the standard LaB₆ sample.

Device fabrication and characterization. The synthesized crystals were partially exfoliated into crystal chips (few μm thick) via scotch tape (Nitto[®] blue tape) method to ensure a flat surface on which deposit the metal contacts and fixed in with a double-side tape in microscope slides. Pt electrodes (60 nm thickness, Pt pellets 99.99% from

Kurt J. Lesker[®]) were deposited (rate 0.4 Å/s) by e-beam evaporation (Kurt J. Lesker Kenosistec[®] evaporator equipped with a cooled sample holder) through a shadow mask, obtaining devices in lateral configuration that have an active channel of 100 μm long and 1 mm wide. Electrical characterization was performed in air and in dark using a Karl Süss – Microtech[®] and EverBeing[®] probe-stations, and a Keithley 2612/2635A source meters in a two-probe configuration controlled by a PC. The measurement protocol was established as previously described.⁴⁴ To avoid spurious effects from electrical spikes, we consider the I_{ON} (LRS) and I_{OFF} (HRS) values for each cycle by taking the average over the read pulse. The I_{ON}/I_{OFF} ratio for each read voltage and sample is determined by the median from the overall of at least 20 cycles. Scanning electron microscopy coupled to Energy dispersive X-Ray spectroscopy (SEM-EDS) measurements of the devices were carried out in a FEI[®] Quanta 250 FEG microscope using 5 kV.

Results and Discussion

Solvent acidolysis crystallization (SAC)^{35,36} of the pure chloride crystal (Cu-1) was performed by the acidolysis of *N*-methylformamide (NMF) in aqueous HCl in the presence of CuCl₂ salt, while in the case of the mixed halide crystals, acidolysis was performed using a mixture of HCl and HBr (Cu-2, Cl:Br ratio of 2.25:1 in feed solution) or only HBr (Cu-3, Cl:Br ratio of 0.3:1 in feed solution) (see experimental section for more details). Photographs of the grown crystals are shown in Figure S1. Note that this crystallization technique obviates the need for a methylammonium halide precursor and instead the organic cation is formed *in-situ* during the crystallization.

We studied the optical properties of all three crystals. The color of the crystals changed from dark yellow to dark brown as the bromine content increased (inset in Figure 1a and Figure S1). The absorbance of the ground crystals (Figure 1a) was obtained by converting the diffuse reflectance spectrum of the ground crystals using the Kubelka-Munk formulae $F(R)=(1-R)^2/2R$ (where R is the diffuse reflectance).⁴⁵ The absorbance spectra show two main features: ligand (halide) to metal charge-transfer transitions at shorter wavelengths and a *d-d* transition around 700 nm, matching previously reported data.²⁵ As expected from the color of the ground crystals, the bandgaps (Figure 1b) showed a gradual decrease from 2.4 eV to 1.8 eV with increased Br incorporation. In order to build the

electronic band diagram of our crystals, we performed ultraviolet photoelectron spectroscopy (UPS) as shown in Figure S2. The positions of the valence band maxima (VBM), with respect to the vacuum level, were calculated to be 6.1, 5.5, and 5.0 eV for Cu-1, Cu-2 and Cu-3 respectively. From the VBM and the bandgap values, the electronic band diagram was calculated and is schematically shown in Figure 1c. No photoluminescence (PL) was observed for all samples, indicating no Cu^{2+} reduction to Cu^+ , which was previously reported to be the origin of the PL at around 525 nm.²⁵

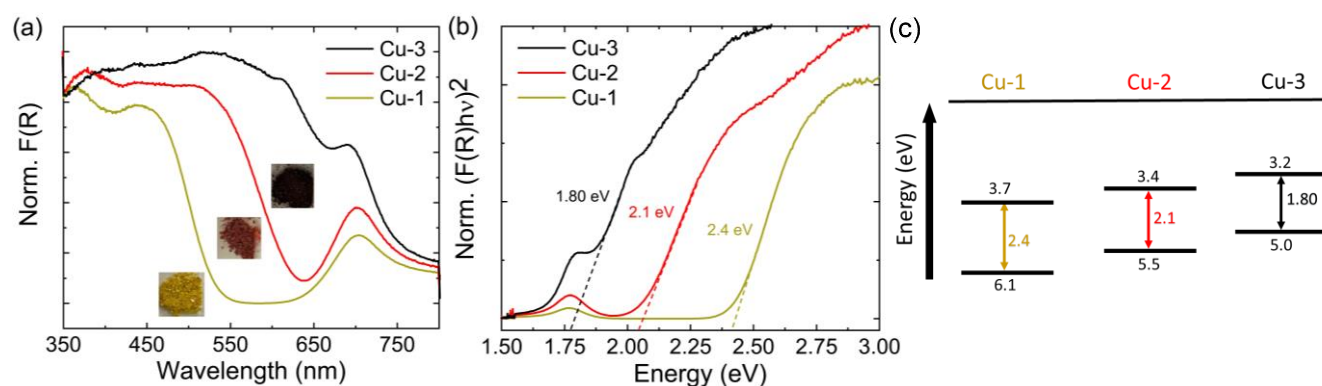


Figure 1. (a) Absorbance of the ground crystals and insets are photographs of the ground crystals. (b) Corresponding Tauc plots and (c) Calculated electronic band diagram.

The thermal stability of the samples was measured by means of differential thermal analysis/thermogravimetric (DTA/TG) coupled with gas–chromatography and mass spectrometry (GC – MS). All three samples started to decompose above 200 °C (Figure S3-S5), consistent with a previous report²⁵. The DTA curves confirmed what is observed in the TG curves. For Cu-1, the decomposition started at 237 °C with the release of CH_3Cl and $\text{N}(\text{CH}_3)_3$ as the major decomposition products. The stability decreased with the introduction of Br, as Cu-2 and Cu-3 decomposed at 224 °C and 198 °C, respectively; for these samples, CH_3Br was also detected. The strength of H-bonds formed between MA groups and halogen ions is essentially related to the electronegativity of the halogen species (Cl = 3.16; Br = 2.96), thus explaining why the measured decomposition temperatures decreases with the increase of Br. For all samples, at $T > 500$ °C the vaporization of the residual inorganic part CuX_2 and/or CuX ($X = \text{Cl}$ and Br) occurred.

The crystalline quality of the pure chloride crystal (Cu-1) was investigated using wide angle X-ray scattering (WAXS). The sample was raster scanned over a $1 \times 1 \text{ mm}^2$ area, in order to obtain an average pattern from a large crystal volume. The resulting spotty 2D pattern shown in Figure 2a (inset) indicates that the sample was a single crystal. The corresponding 1D WAXS profile in Figure 2a was indexed and FP fitted as the monoclinic MA_2CuCl_4 structure reported previously.³¹ Laboratory X-ray powder diffraction (XRPD) patterns of all three ground crystals are shown in Figure 2b. As for the WAXS pattern, the XRPD pattern of Cu-1 ground crystal is in good agreement with the same MA_2CuCl_4 monoclinic structure. The XRPD patterns of the mixed halide crystals (Cu-2 and Cu-3) showed systematic shifts to lower 2theta (Figure 2c), indicating the incorporation of the larger halogen ion (Br) in the crystal structure.²⁵ The incorporation of Br does not deteriorate structural stability of the material indicated by the absence of any secondary phases even after 10 weeks of storage in vacuum oven at 40°C (see Figure S6).

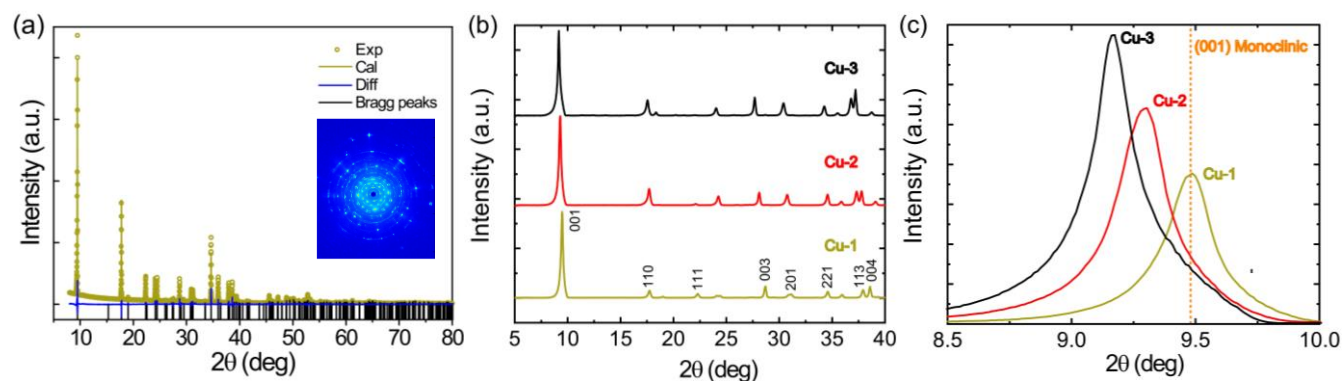


Figure 2. (a) Experimental and calculated 1D-WAXS pattern of Cu-1 corresponding to the 2D WAXS scanning map (inset). (b) Laboratory XRPD diffractograms of ground crystals of pure Cl (Cu-1) and mixed halide compositions (Cu-2 and Cu-3). (c) Zoomed-in powder XRD in the 2Theta range $8.5\text{-}10.0^\circ$ with orange dotted line corresponding to monoclinic MA_2CuCl_4 (ICSD 110695).

The crystal structure of MA_2TCl_4 compounds^{31,32,46-49} (Figure 3, on the left; T = Cu, Mn, Fe, Cd) is essentially an octahedral framework built up of corner sharing $[\text{TCl}_6]^{4+}$ octahedra forming stacked layers along the main axis. Neighboring layers are found to be shifted by half a unit cell in the octahedral plane, giving rise to an ABAB-type

layer stacking. The MA groups are located in between these layers, being connected to the halogen atoms via H-bonds provided by the $-\text{NH}_3$ group (2 bonds with neighboring equatorial Cl atoms and 1 bond with the opposite axial Cl atom; Figure 3, on the right).

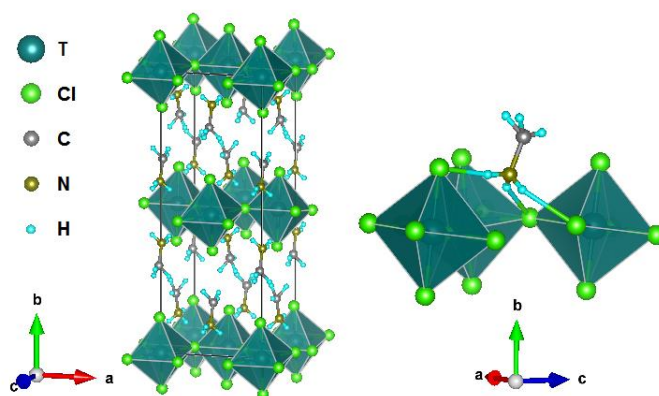


Figure 3. Crystal structure of MA_2TCl_4 compounds (redrawn after standardization of the structural data published by Heger *et al.*⁴⁷)

In order to gain insights about the possible relationship between crystal structure and the physical properties of these materials, an in-depth characterization of the structural properties down to the local scale was carried out. The MA_2TCl_4 compounds are known to crystallize with several polymorphic modifications; we tested several of these structural models with both orthorhombic ($Cmme$ space group) and monoclinic ($P2_1/c$ space group) symmetry. Moreover, in order to take into account the ordered distortion produced by the Jahn-Teller effect, we also tested a different orthorhombic structural model with space group $Pbca$. As a result, the Rietveld refinement using synchrotron XRPD data confirmed that Cu-1 crystallizes with a monoclinic $P2_1/c$ symmetry, whereas the crystal structures of the Br-containing samples (Cu-2 and Cu-3) are well described by the orthorhombic $Pbca$ structural model (Figure S7). Furthermore, Rietveld refinements revealed that all the three samples are characterized by significant amounts of vacancies at the X sites, whose distribution is highly related to the $[\text{Cl}]/[\text{Br}]$ ratio. Figure 4 displays a perspective view of the octahedral layer for the three samples, as calculated from structural data obtained by Rietveld refinements, highlighting the main differences.

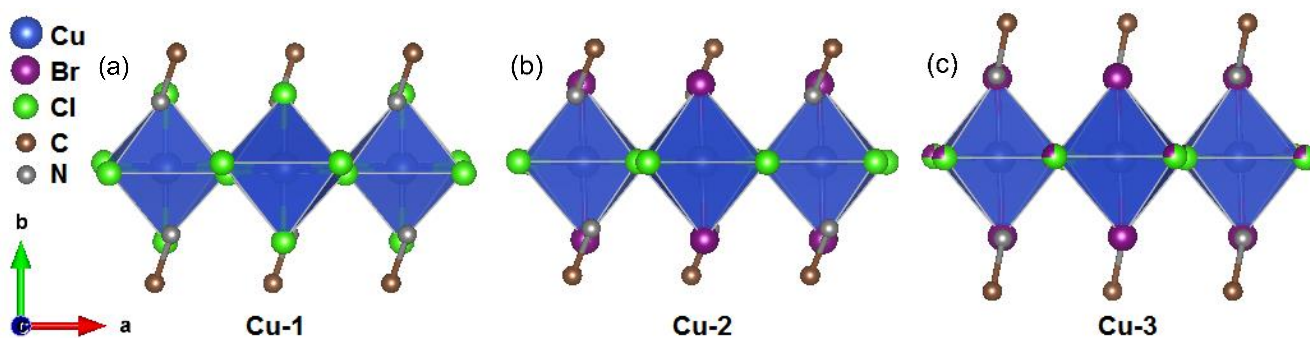


Figure 4. Perspective view of the octahedral layer in (a) Cu-1 (b) Cu-2 and (c) Cu-3 highlighting the different arrangement of the Cl and Br atoms as well as the significant planar corrugation characterizing the sample Cu-1.

Sample Cu-1 exhibits a corrugation of the equatorial plane, which is hardly detectable in samples Cu-2 and Cu-3. Moreover, in Cu-1, significant amounts of vacancies result from the refinement of occupancies at both equatorial and axial positions occupied by Cl atoms. In particular, the equatorial position is characterized by a slightly higher amount of vacancies (~9%), compared to the axial one (~6%).

In sample Cu-2, Br and Cl atoms are located at different sites, likely on account of their different ionic radii (Br: 1.96 Å; Cl: 1.81 Å). In particular, the larger Br atoms are located in axial positions where steric hindrance is reduced; nonetheless, this site is strongly defective, being occupied by only ~73%. Cl atoms are arranged in the much denser populated equatorial plane, characterized by a relatively similar amount of vacancies (~7%) as the equatorial sites in Cu-1. These results are consistent with the structural characterization of $MA_2CuCl_2Br_2$ reported by Willet³², who observed a preferred occupation of Cl atoms for in-plane positions and Cu-Br bonds normal to the plane.

In sample Cu-3, Rietveld refinement indicates that the equatorial positions are fully occupied by both Br and Cl atoms, while vacancies are found only at the axial position. In this context, it is worth noting that no evidence for a significant amount of vacancies was reported in previous structural studies carried out on these materials^{31,32,46-49}; this fact can be ascribed to the different and novel synthesis technique adopted in the present study. As mentioned above, a comparison of the inspected samples reveals that the octahedral layer flattens with the increase of Br content, as the out of plane octahedral tilting angle decreases from ~4.1° in Cu-1, down to ~2.3° in Cu-2 and to ~0.5° in Cu-3.

It is interesting to observe that in samples Cu-2 and Cu-3 the lattice parameters approach a tetragonal metric, with $a \sim c$ (Table 1); a tetragonal structural model was checked in order to ascertain the correct symmetry, however the orthorhombic structural model is preferred in both samples.

The structural models obtained after Rietveld refinements were applied to fit the PDF data (Figure S8); different r -ranges of the $G(r)$ function were fitted in order to compare the medium range structure with the average structure obtained by Rietveld refinements as well as to highlight the deviations at the nearer-neighbors scale. Table 1 compares the main structural parameters as obtained by Rietveld refinements and fitting the $G(r)$ function.

Table 1. Lattice parameters and compositions of the inspected samples as obtained by Rietveld refinements and by fitting the $G(r)$ function.

	Rietveld refinement		G(r) function fitting
	lattice parameters	Composition	lattice parameters
Cu-1	$a = 10.0310(1)$ $b = 7.3628(1)$ $c = 7.2934(1)$ $\gamma = 111.305(8)$	$MA_2Cu(Cl_{1.82})_{eq}(Cl_{1.88})_{ax}$	$a = 10.018(6)$ $b = 7.371(3)$ $c = 7.275(3)$ $\gamma = 111.47(8)$
Cu-2	$a = 7.3429(1)$ $b = 19.0717(1)$ $c = 7.3452(1)$	$MA_2Cu(Cl_{1.86})_{eq}(Br_{1.46})_{ax}$	$a = 7.334(7)$ $b = 19.073(5)$ $c = 7.323(6)$
Cu-3	$a = 7.4204(1)$ $b = 19.3644(1)$ $c = 7.4243(1)$	$MA_2Cu(Cl_{1.46}, Br_{0.54})_{eq}(Br_{1.55})_{ax}$	$a = 7.400(3)$ $b = 19.310(5)$ $c = 7.397(5)$

For sample Cu-1, data obtained by fitting the $G(r)$ function are in fair agreement with that determined with Rietveld refinement. Also for sample Cu-2 the data are quite consistent, even though some significant differences are present, indicating some degree of disordering at the local and short-range scale. On the contrary, data fitting

for the sample Cu-3 using the Rietveld structural model provides a quite poor result. The reason for such a discrepancy between the average short and long structures can be likely ascribed to the intrinsic disorder affecting the crystal structure characterizing this composition. When studying the crystal structure of $\text{MA}_2\text{CuCl}_2\text{Br}_2$, Willet³² observed that Cl and Br atoms were characterized by slightly different coordinates at both equatorial and axial positions, thus indicating a not relaxed structure (in other words, the crystal structure can be described as a superposition and interpenetration of two different structures). Such an intrinsic static disorder is likely the origin of the divergent results obtained for sample Cu-3 from Rietveld refinement (characterizing the average long range structure) and the $G(r)$ function fitting (exploring the structural properties at the local scale). Hence, a different structural model was applied to fit the PDF data, where the equatorial positions of the Br and Cl atoms are characterized by slightly different coordinates. A significant improvement of the fitting was then obtained, indicating a marked difference between the local and long range average structures, therefore confirming the occurrence of a static disorder at the local scale. Moreover, this disorder relaxes to some extent the in-plane steric hindrance, thus possibly explaining why in this sample (Cu-3) the concentration of equatorial vacancies is not significant.

All samples are characterized by quite large values of the thermal parameters associated to halogen atoms, indicating a significant degree of disordering, where Cl and Br atoms are displaced away from their time and space averaged positions, thus pointing to a dynamic motion of the rigid octahedral unit (Figure 4). In particular, sample Cu-2 displays a quite peculiar shape of the thermal parameters characterizing equatorial Cl, strongly elongated along the a -axis. This feature has to be compared with the bond valence sum map⁵⁰, generated by all the points in the unit cell representing possible locations for a Cl^- ion; these bond valence sum maps thus provides insights about possible pathways for ionic conduction. In sample Cu-2, a strong concentration of negative charge in the middle of the equatorial Cl-Cl bond is evident, as shown in Figure 5d.

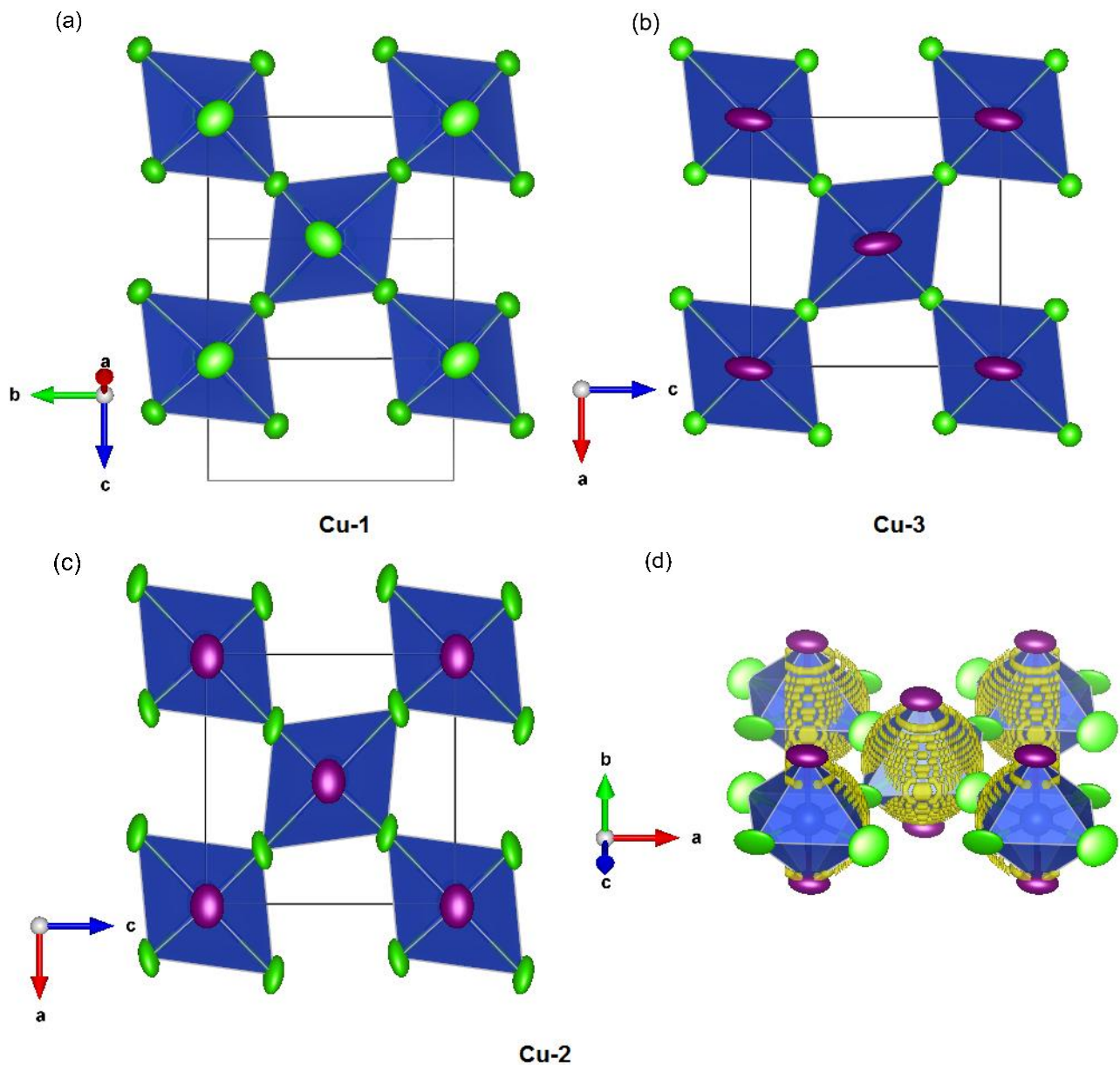


Figure 5. Out of plane view of the octahedral layer where atoms are represented as displacement ellipsoids (90% of probability) in sample (a) Cu-1, (b) Cu-3 and (c) Cu-2. (d) Yellow isosurface of the bond valence sum map of the sample Cu-2 identifies the regions with a calculated oxidation state close to Cl^- (isovalue ± 0.05 valence units).

In order to evaluate how the different halide stoichiometry, and therefore the crystal structure, namely in terms of halide/vacancies arrangement and concentration, can affect the resistive switching properties of the Cu-based crystals, we tested them in proof-of-concept memory devices. As shown in Figure 6a-c, we fabricated lateral

devices using inert Pt as electrodes, to prevent the electrode material from participating in the switching mechanism.⁵¹ Furthermore, using single crystalline material will eliminate possible migration pathways through grain boundaries.^{18,52,53} To assess the suitability of the synthesized Cu-halide based materials for resistive switching, we first performed I-V cycles (Figure 6d-f in log scale, see Figure S9 for the graph in linear scale). The I-V characteristics of the different Cu-based devices measured under a DC voltage sweep (from 0 V \rightarrow 2V \rightarrow 0V \rightarrow -2V \rightarrow 0 V) show a hysteresis (amplitude of the I-V curve at 0.5 V for Cu-1 (1.2 nA), Cu-2 (14.2 nA) and Cu-3 (1.2 nA)), confirming the applicability of these materials for resistive switching. An analysis of the shape and direction of the hysteresis cycles (see the arrows in Figure 6d-f), evidences some differences upon the incorporation of Br in the crystal structure, translated to the type of resistive switching (see SI Note S1 for further discussion).

To better understand the observed behavior, we carried out scanning electron microscopy coupled to energy dispersive X-Ray spectroscopy (SEM-EDS) mapping of the devices after the set-reset measurements. In all cases, the corresponding EDS maps of the Pt, Cu, Cl and Br indicate that there is neither Pt migration nor metallic Cu clusters formation during the device operation (see SI, SEM-EDS mapping on working devices, Figure S10). This suggests that the hysteresis can be only attributed to the Cl and Br ions migration due to halogen vacancies or lattice defects.^{51,54,55} Therefore, halogen ions/vacancies redistribution during the operation of the devices forms the necessary 'conduction path' that leads to lower resistance state (LRS), and can be exploited for memory operation (change from the high resistance state -HRS- (OFF state) to the LRS (ON state)). Under the applied bias, halogen ions migrate towards the positive electrode (due to the driving electric field), and the corresponding halogen vacancies drift in the opposite direction (negative electrode). Considering that the devices are symmetric, Pt/2D Cu-crystal/Pt, the switching mechanism should be activated on the SET and RESET with either positive or negative voltage.^{51,56}

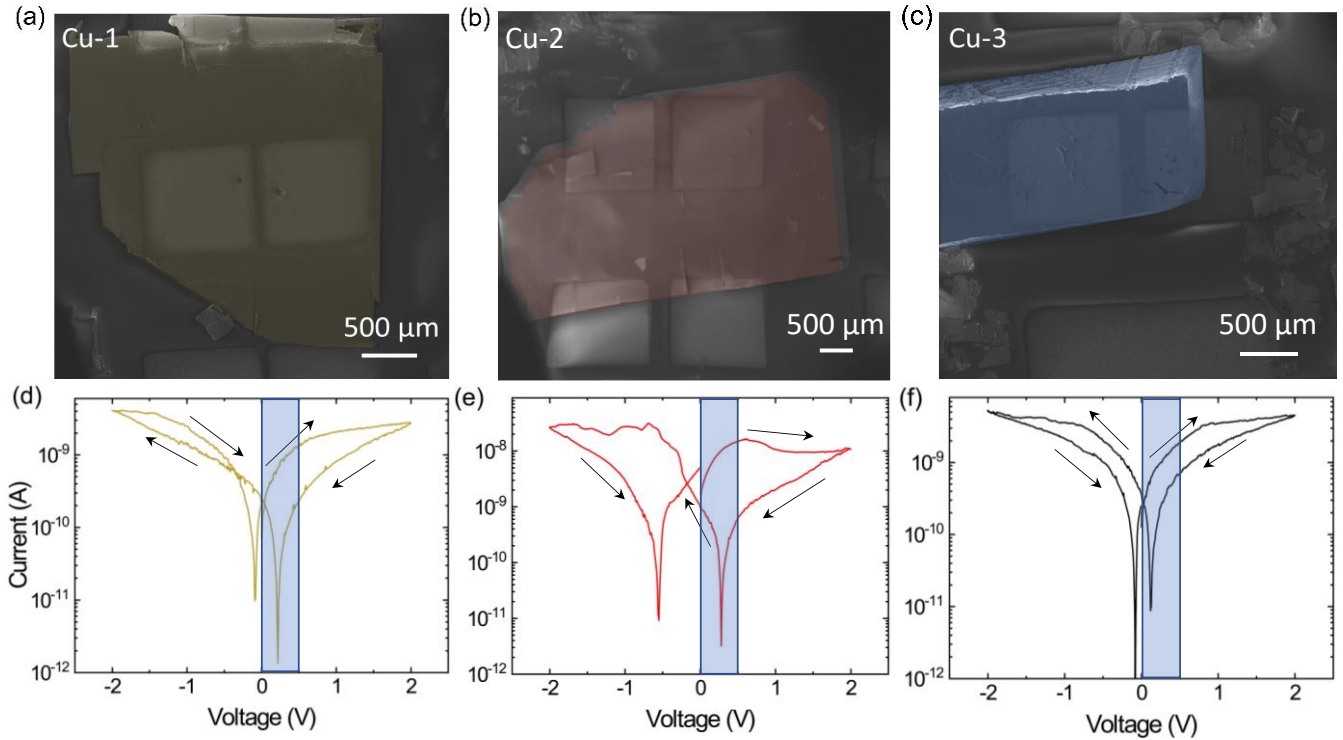


Figure 6. (a-c) Representative SEM images of the Cu-1, Cu-2 and Cu-3 memory devices showing the Pt contacts on top of the crystal chips. (d-f) I–V cycle for representative Pt/Cu-1/Pt, Pt/Cu-2/Pt and Pt/Cu-3/Pt devices indicating with a shaded area the operational voltage range for the memristor read-out.

We carried out tests as a memory device according to the following protocol: a SET pulse is applied to activate the LRS, followed by READ pulses at various voltages to evaluate the minimum voltage at which the system can work and be readable, then a RESET pulse is applied to put back the HRS, followed by READ pulses as before; the current is monitored during the measurement. This SET/READ/RESET/READ run is repeated for at least 20 cycles to evaluate the device stability. We have found that SET (RESET) pulses are effective with a voltage of -2V (+2V), while READ operations are performed at ≤ 0.5 V (Figure 7a-c). From these measurements, we have calculated the ratio of the currents in ON (LRS) and OFF (HRS) states (after SET and RESET operation, respectively) (Figure 7d-f). We consistently find a higher ratio at $V_{\text{READ}} = 0.1$ V in all systems, which is compatible with low-power consumption device requirements. Comparing the different samples, it is observed that the Cu-2 crystal showed the best performance with an $I_{\text{ON}}/I_{\text{OFF}}$ ratio of ~ 10 , while Cu-1 ($I_{\text{ON}}/I_{\text{OFF}}$ ratio of ~ 4) and Cu-3 ($I_{\text{ON}}/I_{\text{OFF}}$ ratio of ~ 2) values are lower. In fact, the higher response in terms of ON/OFF ratio yielded by Cu-2 is

supported by the observation of a large hysteresis in the I-V curve (see Figure 6d, 14.2 nA difference between high and low current state at 0.5 V). Considering the higher performance in Cu-2 devices, we carried out additional measurements on this sample showing an endurance of ~250 cycles (Figure S11).

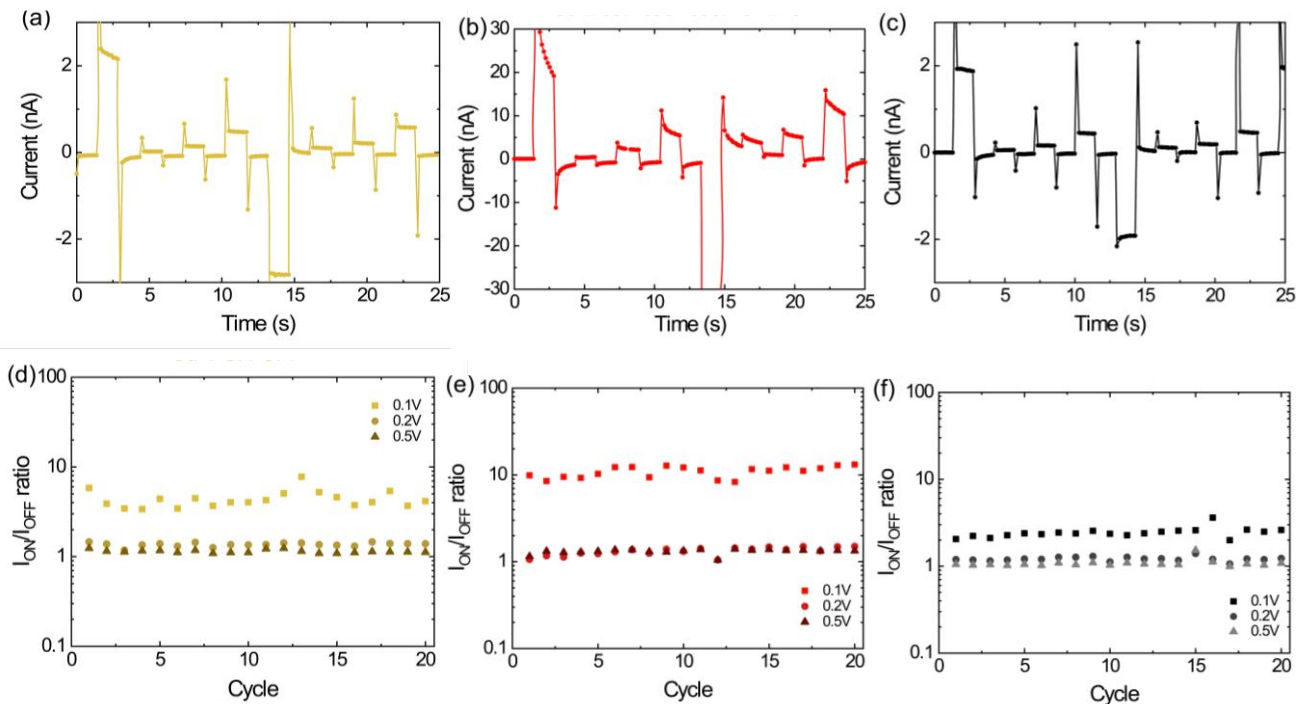


Figure 7. (a-c) Time trace of voltage current during the reset/read/set/read procedure for the Pt/Cu-1/Pt, Pt/Cu-2/Pt and Pt/Cu-3/Pt devices. Set/reset voltage values are -2 V and $+2$ V, respectively, and the read voltages are 0.1V, 0.2V and 0.5V (read pulse 1 s). (d-f) The corresponding I_{ON}/I_{OFF} ratio values acquired over 20 set/reset cycles.

It has been previously reported that a higher Schottky barrier should result in an enhanced ON/OFF⁵⁷, which is not the case in our devices, considering the electronic band diagram in Figure 1c and the Pt work function (6.35 eV)⁵⁷, assuming our crystals are intrinsic semiconductors. An explanation for the differences in hysteresis and ON/OFF ratios can instead be established on the bases of stoichiometry and composition of the crystals as well as on the crystal structure.^{4,15,58} Firstly, note that there is a change in the crystal structure from monoclinic (Cu-1) to orthorhombic (Cu-2), which may promote a favorable environment for the halogen migration, as in other perovskite-structured compounds.⁵⁹ It is also important to note that all samples are halogen deficient as evidenced

by Rietveld refinement using synchrotron XRPD data, which means the presence of vacancies or interstitial defects in the structure, and therefore provides a favorable condition for ion mobility.^{13,17,60} The concentration and location of these vacancies at the distinct crystallographic sites play a role in defining the ion migration pathways and promoting the transport. As mentioned before, in both Cu-1 and Cu-2, relatively similar concentrations of equatorial vacancies are present. However, in Cu-2, all equatorial sites are located almost in the same plane, probably facilitating the halogen ion/vacancy diffusion, unlike in Cu-1, where the corrugated octahedral plane results in the two nearest neighboring equatorial Cl atoms being at significantly different heights from the *bc* plane, thus reducing the possibility of atomic diffusion along the plane. Moreover, the elongation of the ellipsoids along the *a*-axis in Cu-2 suggests that, in this sample, the Cl atoms can diffuse parallel to the *a*-direction, thanks to the significant concentration of equatorial vacancies and the fact that all equatorial Cl atoms are located almost in a same plane (Figure 4). This anisotropic thermal motion was previously reported to indicate the preferred oxide ion migration pathway.^{34,61} In addition, in Cu-2, the bond valence sum maps point to an ionic conduction mechanism mainly involving the migration of Cl ions along the equatorial plane. This scenario is fully consistent with theoretical calculations in 3D halide perovskites.⁶² On the other hand, Cu-3 displayed smaller hysteresis and lower ON/OFF ratio with respect to Cu-2. This can be explained by the amount of vacancies at the equatorial positions that is negligible in Cu-3. Hence, the in-plane diffusion of halogen ions is prevented or at least strongly hindered. These results indicate that, in Cu-3, the possible ion/vacancy migration path is axial-to-equatorial, and suggests that it is of a higher energy barrier compared to the expected equatorial-to-equatorial ion migration in Cu-2. Indeed, it has been previously reported through density functional theory (DFT) that, in 3D MAPbBr₃, the bromine ion migration from equatorial-to-axial sites is of higher activation energy compared to equatorial-to-equatorial migration.²⁰ Similarly, in layered oxide perovskites, it was reported that vacancy migration is more favored between two adjacent equatorial positions.³³ Our experimental results highlight that the previously reported suppressed ion migration in halide perovskites through compositional engineering^{11,12} or through dimensionality reduction^{63,64} could be indeed due to variations in the local crystal structure.

The best results we achieved with Cu-2 (I_{ON}/I_{OFF} ratio of ~ 10 at $V_{READ} = 0.1$ V with SET/RESET ± 2 V) compare well with the literature involving 2D Pb-based materials and non-active electrodes (*i.e.*, devices in which only

halide migration could take place), as NiO/2D BA₂PbBr₄/ZnO/FTO (where BA = butylammonium, I_{ON}/I_{OFF} ratio of <10 at V_{READ} = 0.5 V with SET/RESET 1.2/-2V)⁶⁵, and graphene/2D PEA₂PbBr₄ (single crystal)/Au (I_{ON}/I_{OFF} ratio of 10 at I_{READ} = 10 pA with SET/RESET ±2.8V).⁶⁶ Nevertheless, there is room for improvement in device configuration and design, as it has already been demonstrated with the extensively studied 3D MAPbI₃-based perovskite devices.⁶⁷

Conclusion

Adopting a combined study of average/local structural characterization and detailed electrical measurements, we shine light on the interrelationships between structure and efficiency of ion migration in layered methylammonium copper halide materials (MA₂CuX₄). In our experimental investigation, we observe that the presence of mixed Cl/Br anions not only influences the optical bandgap and thermal stability but also induces intricate local structural changes that affect the ion migration and, consequently, the ON/OFF ratio in the memory devices. Through comparing the structural data obtained by detailed XRPD-PDF analysis and our devices performances, we identify several favorable conditions for halogen ion/vacancy mobility in sample Cu-2 (MA₂Cu(Cl_{1.86})_{eq}(Br_{1.46})_{ax}): (i) some halogen ion vacancies are located in the equatorial octahedral sites; and (ii) all equatorial sites are located almost in the same plane; (iii) elongation of the equatorial Cl ellipsoids along the *a*-axis; and (iv) its bond valence sum maps show a strong concentration of negative charge in the middle of the equatorial Cl-Cl bond, which all lead to a better performance in terms of I_{ON}/I_{OFF} ratio. These experimental results made on single crystalline samples highlights the need to study detailed structural factors that could affect ionic migration in perovskite and perovskite-related compounds, which is important for the performance of memristor and optoelectronic devices.

Acknowledgements

The authors thank Dr A. Toma for the access to the IIT clean room facilities, and C. Biagini for support during the evaporation procedures. B.M-G. acknowledges the funding from the European Union's Horizon 2020 research

and innovation programme under grant agreement no. 785219 (GrapheneCore2) and Diputación de Gipuzkoa (Spain) in the frame of Gipuzkoa Fellows Program. A.M and F.L. thank European Synchrotron Radiation Facility for beamtime (proposal HC-3840) and Dr. W. Bogodi for assistance during data collection at ID22.

References

- 1 M. H. Futscher, J. M. Lee, L. McGovern, L. A. Muscarella, T. Wang, M. I. Haider, A. Fakharuddin, L. Schmidt-Mende and B. Ehrler, *Mater. Horizons*, 2019, **6**, 1497–1503.
- 2 T. Zhang, H. Chen, Y. Bai, S. Xiao, L. Zhu, C. Hu, Q. Xue and S. Yang, *Nano Energy*, 2016, **26**, 620–630.
- 3 J. W. Lee, S. G. Kim, J. M. Yang, Y. Yang and N. G. Park, *APL Mater.*, , DOI:10.1063/1.5085643.
- 4 Y. Yuan and J. Huang, *Acc. Chem. Res.*, 2016, **49**, 286–293.
- 5 S. Meloni, T. Moehl, W. Tress, M. Franckeviius, M. Saliba, Y. H. Lee, P. Gao, M. K. Nazeeruddin, S. M. Zakeeruddin, U. Rothlisberger and M. Graetzel, *Nat. Commun.*, , DOI:10.1038/ncomms10334.
- 6 P. Vashishtha and J. E. Halpert, *Chem. Mater.*, 2017, **29**, 5965–5973.
- 7 H. Kim, J. S. Han, S. G. Kim, S. Y. Kim and H. W. Jang, *J. Mater. Chem. C*, 2019, **7**, 5226–5234.
- 8 B. Li, W. Hui, X. Ran, Y. Xia, F. Xia, L. Chao, Y. Chen and W. Huang, *J. Mater. Chem. C*, 2019, **7**, 7476–7493.
- 9 J. S. Han, Q. Van Le, J. Choi, H. Kim, S. G. Kim, K. Hong, C. W. Moon, T. L. Kim, S. Y. Kim and H. W. Jang, *ACS Appl. Mater. Interfaces*, 2019, **11**, 8155–8163.
- 10 Y. Shan, Z. Lyu, X. Guan, A. Younis, G. Yuan, J. Wang, S. Li and T. Wu, *Phys. Chem. Chem. Phys.*, 2018, **20**, 23837–23846.
- 11 R. García-Rodríguez, D. Ferdani, S. Pering, P. J. Baker and P. J. Cameron, *J. Mater. Chem. A*, 2019, **7**, 22604–22614.
- 12 D. W. Ferdani, S. R. Pering, D. Ghosh, P. Kubiak, A. B. Walker, S. E. Lewis, A. L. Johnson, P. J. Baker, M. S. Islam and P. J. Cameron, *Energy Environ. Sci.*, 2019, **12**, 2264–2272.
- 13 C. Eames, J. M. Frost, P. R. F. Barnes, B. C. O'Regan, A. Walsh and M. S. Islam, *Nat. Commun.*, 2015,

- 6, 2–9.
- 14 T. Y. Yang, G. Gregori, N. Pellet, M. Grätzel and J. Maier, *Angew. Chemie - Int. Ed.*, 2015, **54**, 7905–7910.
- 15 A. Oranskaia, J. Yin, O. M. Bakr, J. L. Brédas and O. F. Mohammed, *J. Phys. Chem. Lett.*, 2018, **9**, 5474–5480.
- 16 C. Lan, S. Zhao, J. Luo and P. Fan, *Phys. Chem. Chem. Phys.*, 2018, **20**, 24339–24344.
- 17 D. Barboni and R. A. De Souza, *Energy Environ. Sci.*, 2018, **11**, 3266–3274.
- 18 D. Meggiolaro, E. Mosconi and F. De Angelis, *ACS Energy Lett.*, 2019, **4**, 779–785.
- 19 J. Chen, D. Lee and N. G. Park, *ACS Appl. Mater. Interfaces*, 2017, **9**, 36338–36349.
- 20 N. Rybin, D. Ghosh, J. Tisdale, S. Shrestha, M. Yoho, D. Vo, J. Even, C. Katan, W. Nie, A. J. Neukirch and S. Tretiak, *Chem. Mater.*, 2020, **32**, 1854–1863.
- 21 J. M. Azpiroz, E. Mosconi, J. Bisquert and F. De Angelis, *Energy Environ. Sci.*, 2015, **8**, 2118–2127.
- 22 J. L. Minns, P. Zajdel, D. Chernyshov, W. Van Beek and M. A. Green, *Nat. Commun.*, 2017, **8**, 1–5.
- 23 C. C. Stoumpos, C. D. Malliakas and M. G. Kanatzidis, *Inorg. Chem.*, 2013, **52**, 39.
- 24 L. Mao, H. Tsai, W. Nie, L. Ma, J. Im, C. C. Stoumpos, C. D. Malliakas, F. Hao, M. R. Wasielewski, A. D. Mohite and M. G. Kanatzidis, *Chem. Mater.*, 2016, **28**, 7781–7792.
- 25 D. Cortecchia, H. A. Dewi, J. Yin, A. Bruno, S. Chen, T. Baikie, P. P. Boix, M. Grätzel, S. Mhaisalkar, C. Soci and N. Mathews, *Inorg. Chem.*, 2016, **55**, 1044–1052.
- 26 P. Pandey, N. Sharma, R. A. Panchal, S. W. Gosavi and S. Ogale, *ChemSusChem*, 2019, **12**, 3742–3746.
- 27 S. Y. Kim, J. M. Yang, E. S. Choi and N. G. Park, *Adv. Funct. Mater.*, 2020, **2002653**, 1–9.
- 28 J. J. M. Steijger, E. Frikkee, L. J. De Jongh and W. J. Huiskamp, *Phys. B+C*, 1984, **123**, 271–283.
- 29 R. D. Willett, O. L. Liles and C. Michelson, *Inorg. Chem.*, 1967, **6**, 1885–1889.
- 30 J. J. M. Steijger, E. Frikkee and L. J. De Jongh, *J. Magn. Magn. Mater.*, 1979, **14**, 152–154.
- 31 I. Pabst, H. Fuess and J. W. Bats, *Acta Crystallogr. Sect. C Cryst. Struct. Commun.*, 1987, **43**, 413–416.
- 32 R. D. Willett, *Acta Crystallogr. Sect. C*, 1991, **47**, 1081–1082.
- 33 C. Tealdi, C. Ferrara, P. Mustarelli and M. S. Islam, *J. Mater. Chem.*, 2012, **22**, 8969–8975.

- 34 A. C. Tomkiewicz, M. Tamimi, A. Huq and S. McIntosh, *J. Mater. Chem. A*, 2015, **3**, 21864–21874.
- 35 J. Shamsi, A. L. Abdelhady, S. Accornero, M. Arciniegas, L. Goldoni, A. R. S. Kandada, A. Petrozza and L. Manna, *ACS Energy Lett.*, 2016, **1**, 1042–1048.
- 36 K. M. Boopathi, B. Martín-garcía, A. Ray, M. Pina, S. Marras, M. I. Saidaminov, F. Bonaccorso, F. Di Stasio, E. H. Sargent, L. Manna and A. L. Abdelhady, *ACS Energy Lett.*, 2020, 642–649.
- 37 D. Altamura, R. Lassandro, F. A. Vittoria, L. De Caro, D. Siliqi, M. Ladisa and C. Giannini, *J. Appl. Crystallogr.*, 2012, **45**, 869–873.
- 38 D. Siliqi, L. De Caro, M. Ladisa, F. Scattarella, A. Mazzone, D. Altamura, T. Sibillano and C. Giannini, *J. Appl. Crystallogr.*, 2016, **49**, 1107–1114.
- 39 F. Locardi, E. Canepa, S. Villa, I. Nelli, C. Lambruschini, M. Ferretti and F. Canepa, *J. Anal. Appl. Pyrolysis*, 2018, **132**, 11–18.
- 40 R. A. Young, “*The Rietveld Method*”, *Chap. 1, IUCr Monographs on Crystallography vol 5, Oxford, 1993*, Oxford University Press.
- 41 P. Juhás, T. Davis, C. L. Farrow and S. J. L. Billinge, *J. Appl. Crystallogr.*, 2013, **46**, 560–566.
- 42 B. H. Toby and T. Egami, *Acta Crystallogr. Sect. A*, 1992, **48**, 336–346.
- 43 C. L. Farrow, P. Juhas, J. W. Liu, D. Bryndin, E. S. Božin, J. Bloch, T. Proffen and S. J. L. Billinge, *J. Phys. Condens. Matter*, 2007, **19**, 335219.
- 44 B. Martín-García, D. Spirito, R. Krahne and I. Moreels, *J. Mater. Chem. C*, 2018, **6**, 13128–13135.
- 45 H. Zhou, X. Cui, C. Yuan, J. Cui, S. Shi, G. He, Y. Wang, J. Wei, X. Pu, W. Li, D. Zhang, J. Wang, X. Ren, H. Ma, X. Shao, X. Wei, J. Zhao, X. Zhang and J. Yin, *ACS Omega*, 2018, **3**, 13960–13966.
- 46 G. Chapuis, R. Kind and H. Arend, *Phys. status solidi*, 1976, **36**, 285–295.
- 47 G. Heger, D. Mullen and K. Knorr, *Phys. Status Solidi*, 1975, **31**, 455–462.
- 48 G. Chapuis, H. Arend and R. Kind, *Phys. status solidi*, 1975, **31**, 449–454.
- 49 I. Pabst, J. Karolyi, H. Fuess and M. Couzi, *Phys. Status Solidi*, 1996, **155**, 341–352.
- 50 I. D. Brown, *Chem. Rev.*, 2009, **109**, 6858–6919.
- 51 Y. Zhu, P. Cheng, J. Shi, H. Wang, Y. Liu, R. Xiong, H. H. Ma and H. H. Ma, *Adv. Electron. Mater.*,

- 2020, **6**, 1–8.
- 52 J. S. Yun, J. Seidel, J. Kim, A. M. Soufiani, S. Huang, J. Lau, N. J. Jeon, S. Il Seok, M. A. Green and A. Ho-Baillie, *Adv. Energy Mater.*, 2016, **6**, 1–8.
- 53 A. Younis, L. Hu, P. Sharma, C. Lin, Y. Mi, X. Guan, D. Zhang, Y. Wang, T. He, X. Liu, B. Shabbir, S. Huang, J. Seidel and T. Wu, *Adv. Funct. Mater.*, 2020, 2002948.
- 54 A. Solanki, A. Guerrero, Q. Zhang, J. Bisquert and T. C. Sum, *J. Phys. Chem. Lett.*, 2020, **11**, 463–470.
- 55 S. Ge, X. Guan, Y. Wang, C. H. Lin, Y. Cui, Y. Huang, X. Zhang, R. Zhang, X. Yang and T. Wu, *Adv. Funct. Mater.*, 2020, **30**, 1–9.
- 56 R. Waser, D. Ielmini, H. Akinaga, H. Shima, H.-S. P. Wong, J. J. Yang and S. Yu, *Resist. Switch.*, 2016, 1–30.
- 57 J. Y. Seo, J. Choi, H. S. Kim, J. Kim, J. M. Yang, C. Cuhadar, J. S. Han, S. J. Kim, D. Lee, H. W. Jang and N. G. Park, *Nanoscale*, 2017, **9**, 15278–15285.
- 58 A. Senocrate and J. Maier, *J. Am. Chem. Soc.*, 2019, **141**, 8382–8396.
- 59 C. A. J. Fisher, N. Kuganathan and M. S. Islam, *J. Mater. Chem. A*, 2013, **1**, 4207–4214.
- 60 Z. Xiao, Y. Yuan, Y. Shao, Q. Wang, Q. Dong, C. Bi, P. Sharma, A. Gruverman and J. Huang, *Nat. Mater.*, 2015, **14**, 193–197.
- 61 M. Yashima, N. Sirikanda and T. Ishihara, *J. Am. Chem. Soc.*, 2010, **132**, 2385–2392.
- 62 D. J. Xue, Y. Hou, S. C. Liu, M. Wei, B. Chen, Z. Huang, Z. Li, B. Sun, A. H. Proppe, Y. Dong, M. I. Saidaminov, S. O. Kelley, J. S. Hu and E. H. Sargent, *Nat. Commun.*, 2020, **11**, 1–8.
- 63 J. Cho, J. T. DuBose, A. N. T. Le and P. V. Kamat, *ACS Mater. Lett.*, 2020, **2**, 565–570.
- 64 X. Xiao, J. Dai, Y. Fang, J. Zhao, X. Zheng, S. Tang, P. N. Rudd, X. C. Zeng and J. Huang, *ACS Energy Lett.*, 2018, **3**, 684–688.
- 65 M. Kumar, H. S. Kim, D. Y. Park, M. S. Jeong and J. Kim, *ACS Appl. Mater. Interfaces*, 2018, **10**, 12768–12772.
- 66 H. Tian, L. Zhao, X. Wang, Y. W. Yeh, N. Yao, B. P. Rand and T. L. Ren, *ACS Nano*, 2017, **11**, 12247–12256.

67 K. Yan, M. Peng, X. Yu, X. Cai, S. Chen, H. Hu, B. Chen, X. Gao, B. Dong and D. Zou, *J. Mater. Chem. C*, 2016, **4**, 1375–1381.